Alma Mater Studiorum Università di Bologna
Archivio istituzionale della ricerca

Characterization of very-large-scale motions in high-Re pipe flows

(Article begins on next page)

30 June 2024

Characterization of very-large-scale motions in high-Re pipe flows

Stefano Discetti[a,*], Gabriele Bellani[b], Ramis Örlü[b,c], Jacopo Serpieri[d], Carlos Sanmiguel Vila[a], Marco Raiola[a], Xiaobo Zheng[b,e], Lucia Mascotelli[b], Alessandro Talamelli[b], Andrea Ianiro[a]

[a]*Aerospace Engineering Research Group, Universidad Carlos III de Madrid, Avda. Universidad 30, 28911, Leganes, Spain*
[b] *Università di Bologna, Dipartimento Ingegneria Industriale, Forlì, Italy*
[c]*Linné FLOW Centre, Dept. of Mechanics, KTH Royal Institute of Technology, Stockholm, Sweden*
[d]*Delft University of Technology, AWEP Department, Aerodynamics, Delft, The Netherlands*
[e]*School of Naval Architecture, Ocean Civil Engineering, Shanghai Jiao Tong University, Shanghai, China.*

Abstract

Very-large-scale structures in pipe flows are characterized using an extended Proper Orthogonal Decomposition (POD)-based estimation. Synchronized non-time-resolved Particle Image Velocimetry (PIV) and time-resolved, multi-point hot-wire measurements are integrated for the estimation of turbulent structures in a pipe flow at friction Reynolds numbers of 9500 and 20000. This technique enhances the temporal resolution of PIV, thus providing a time-resolved description of the dynamics of the large scale motions. The experiments are carried out in the CICLoPE facility. A novel criterion for the statistical characterization of the large scale motions is introduced, based on the time-resolved dynamically-estimated POD time coefficients. It is shown that high-momentum events are less persistent than low-momentum events, and tend to occur closer to the wall. These differences are further enhanced with increasing Reynolds number.

Keywords: Pipe flow; Boundary layer; POD; Very Large Scale Motions.

1. Introduction

Dimensional arguments lead to assume a universal behavior – i.e. independent of Reynolds number and geometry – in the near-wall region of wall-bounded turbulent flows, when using suitable viscous quantities for scaling (such as the friction velocity u_τ and the viscous length-scale ℓ_*). A most-celebrated evidence of this universality is the law of the wall, which incorporates the logarithmic mean velocity profile (see e.g. Ref. [1] and [2]). However, with the increasing availability of accurate high-Reynolds-number data, not only concerning the mean flow, but also higher-order statistics of turbulent fluctuations, this view has been progressively challenged (see, e.g. Refs. [3, 4, 5, 6, 7]).

The scaling of the higher-order velocity statistics is, for instance, controversial. Recent measurements suggest that, in a pipe flow, all the components of the Reynolds stress tensor adhere to the scaling obtained from Townsends attached eddy hypothesis [7]. However, the viscous scaling fails to collapse the inner peak of the streamwise velocity variance [8, 9]. Moreover, spectral analysis of the turbulent fluctuations shows that the outer region is dominated by very low frequency motions, whose magnitude and size do not collapse in inner nor in outer scaling [6, 10]. These scaling anomalies undermine the grounds for near-wall turbulence descriptions based on complete scale separation.

Hence, the interaction between small scales and geometry and Reynolds-dependent large scales should be taken into account.

The role of coherent structures is believed to be particularly relevant in this picture. More specifically, a key role in the mechanism of turbulent production appears to be played by structures extending over several outer-length scales, referred to as large-scale motions (LSMs) and very-large-scale motions (VLSMs) [11, 12, 13]. LSMs and VLSMs carry more than half of the kinetic energy and Reynolds shear stresses in a fully developed turbulent pipe flow [14]. These findings go along with the attached-eddy-hypothesis [15], which attributes a large fraction of the turbulent kinetic energy in the flow to coherent flow patterns that are attached to the wall [16]. Although, wall-attached structures are found to contribute the most to the skin-friction generation, the fraction due to LSM and VLSM is not negligible [17]. Additionally, several studies have shown that these large structures, although arising in the outer region, interact systematically with the inner layer by modulating the amplitude of the near-wall fluctuations [8, 18]. The aforementioned findings highlight, that understanding the dynamics of LSMs and VLSMs can pave the way to prediction [19] and control [20] of the near-wall turbulence behavior and hence skin-friction generation using only the information extracted from the outer region. Consequently, recent efforts have been focused on the dynamics of large-scale outer-layer structures and on the quantification of their interaction with the small-scale

---
*Corresponding author
Email address: `sdiscett@ing.uc3m.es` (Stefano Discetti)

near-wall eddies [21].

The origin and definition of LSMs and VLSMs is controversial. A widely accepted picture of LSMs is of patches of uniform momentum, with size of the order of 2-3 outer scales [11]. The origin of LSMs can be ascribed to the alignment of vortex packets travelling together at the same convective velocity [22]. VLSMs (also referred as superstructures in external flows [18]) have similar features, only being larger in size (even larger than 10 outer scales) and with characteristic meandering behaviour. The origin of VLSMs is still rather unclear. Kim and Adrian [11] explained their existence as the result of the merging of several LSMs. Subsequent studies [23, 24] demonstrated that the dynamics of the structures in the outer layer is independent of smaller structures near the wall. More recently, Hellström et al. [25] observed the presence of a structure consisting of wall-attached and wall-detached large-scale structures, which appears to be related to the VLSMs formation. Hellström et al. [26] demonstrated that the radial POD (Proper Orthogonal Decomposition) modes exhibit a self-similar behavior, where a single length scale is sufficient to represent the complete structure.

Several challenges have to be undertaken for the direct observation and measurement of VLSMs. The observation of the VLSMs requires a large field of view and a high spatio-temporal resolution, as well as a long acquisition time in order to ensure sufficient statistical convergence. The requirements in terms of spatial and velocity dynamic range challenges state-of-the-art field velocimetry techniques, with the ratio between the largest and smallest measurable scale of the order of 100, and even smaller for volumetric velocimetry [27]. Additionally, temporal resolution is difficult to achieve due to hardware limitations. In this work a quantitative characterization of VLSMs is achieved by exploiting the temporal resolution of hot-wire (HW) probes and the spatial resolution of non-time-resolved planar particle image velocimetry (PIV). Discetti et al. [28] recently assessed a methodology for the filtered dynamic estimation of turbulent flows to blend spatially and temporally-resolved measurements. The approach is based on the extended Proper Orthogonal Decomposition [29] Linear Stochastic Estimation (LSE) tools as in Refs. [30, 31, 32].

The experiments are carried out in the Long Pipe Facility at the Center for International Cooperation in Long Pipe Experiments (CICLoPE [33]), a facility that allows to explore a wide Reynolds-number range, while keeping the smallest scales of turbulence resolvable e.g. with standard HW probes. The experiments are performed with a synchronized acquisition of PIV snapshots and HW sequences from a rake of 5 probes located immediately downstream of the PIV measurement domain. The experimental setup and the methodology are outlined in Sec. 2. An objective *machine-learned* criterion to define a LSM based on the results of Proper Orthogonal Decomposition analysis of the PIV fields is outlined in Sec. 3. The long data sequences allow a full statistical characterization of the

very-large-scale motions in the pipe. A novel modal analysis technique (Extended POD) is applied to assess location and duration of these motion. Furthermore, we can identify the Reynolds-number-dependent characteristics of low- and high-momentum motions.

2. Methodology

2.1. The Long Pipe facility

The Long Pipe facility at CICLoPE is a 111.15 m long pipe embedded in a closed-loop circuit (see fig. 1). The inner diameter of the pipe is of $D = 2R = 901$ mm, and the resulting length to diameter ratio is $L/D \approx 124$. The facility includes a heat exchanger (temperature controlled within $\pm 0.1°C$), a 4-stage axial fan, a settling chamber with honeycomb and 5 anti-turbulence screens, and a 4:1 contraction. The range of friction Reynolds numbers (Re_τ) that can be currently be achieved is from 3.000 to 40.000. The corresponding viscous length scales in this range vary between 88 and 11 μm which is sufficiently large to avoid spatial filtering effects with standard hot-wire probes. Each of the 22 pipe sections has 4 pressure ports and 4 access locations at 90° of angular spacing. The streamwise pressure gradient dP/dx is obtained by fitting a linear trend to the static pressure measurements in the range $80 < x/D < 110$. The wall shear stress τ_w is estimated as $(D/4)(dP/dx)$. The resulting friction velocity is obtained as $u_\tau = \sqrt{\tau_w/\rho}$. An L-shaped Prandtl tube is mounted 5 pipe diameters upstream of the measurement stations to monitor the centerline speed U_c. The bulk velocity U_{bulk} is computed, instead, from the pressure drop across the contraction.

2.2. Measurement setup

The experiments are performed at a measurement station located at $L/D \approx 120$, where the flow is fully developed (i.e. the pressure drop is balanced by the skin friction and the mean velocity is invariant in the streamwise direction). Specifically, the mean pressure gradient is found to be linear starting from at least $x/D = 50$ and previous measurements of the mean streamwise velocity profiles at $x/D = 116$ and $x/D = 123$ have been found to be indistinguishable, thereby justifying our current measurements between these two streamwise stations (see chapter 3 of the PhD thesis by Fiorini [34] for more details). Single-wire HW probes are mounted on a rake at wall-normal positions following an approximate logarithmic distribution: $y/R = 0.085, 0.17, 0.26, 0.43, 0.77$, as sketched in Figure 2. The blockage produced by the probes and the supporting structure has been estimated to be negligible (below 1%). The probes are manufactured by soldering a fully-etched Platinum wire with a nominal diameter of 5 μm to the conical steel prongs. The length of the sensitive wire is 1 mm to keep the wire aspect ratio equal to 200. Carbon fiber probe holders are used to reduce the effect of mechanical vibrations on the measurements. The overall

2

	Re_τ	U_c [m/s]	U_{bulk} [m/s]	u_τ [m/s]	ℓ_* [μm]	ρ [kg/m^3]	ν [10^{-6} m^2/s]
Case 1	9500	9.4	8	0.32	48	1.20	15.1
Case 2	20000	20.7	18.2	0.68	23	1.19	15.3

Table 1: Experimental flow parameters: friction Reynolds number (Re_τ), centreline (U_c), bulk (U_b) and friction (u_τ) velocities, viscous length scale (ℓ_*), density (ρ) and kinematic viscosity (ν) of the fluid.

	Re_τ	f_{HW} [Hz]	f_{PIV} [Hz]	t [s]	$(tU_b)/R$	N_t	N_s
Case 1	9500	10000	5	1200	21280	600	10000
Case 2	20000	20000	5	1200	48450	600	10000

Table 2: Acquisition settings: sampling frequency of HW (f_{HW}) and PIV (f_{PIV}), sampling time of the HW probes in dimensional (t) and non-dimensional form (tU_b/R), number of HW samples associated to each PIV snapshot (N_t) and total number of PIV snapshots (N_s). Data were captured in two runs per case, each one of duration t.
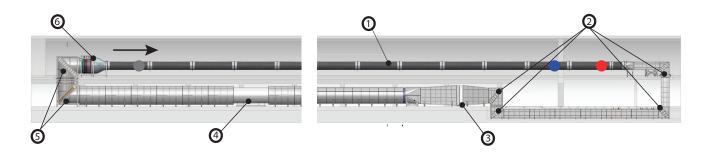

Figure 1: Overview of the Long Pipe (LP) facility: 1) The carbon-fiber pipe 2) Rectangular expanding corners 3) Heat Exchanger 4) Fan assembly 5) Round corners 6) Settling chamber and Convergent assembly. The arrow shows the flow direction. The red, blue and gray markers indicate the location of the measurement station, of the Pitot tube and the PIV seeding particles inlet, respectively.
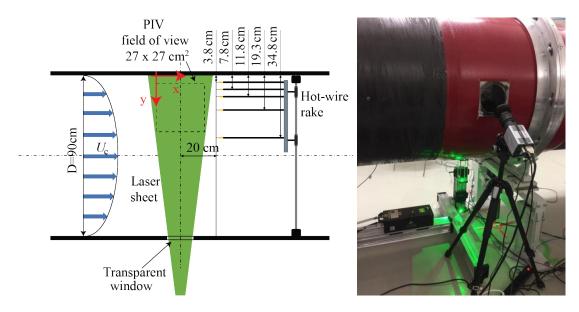

Figure 2: Left: Schematic of: hot-wire rake location, PIV image area, origin and orientation of the coordinate system. Right: PIV imaging setup.

blockage area of the rake is $< 3\%$ of the pipe cross-section area, which ensures minimal intrusivity. The hot-wires are operated through a Dantec StreamLine 90N10 frame with 90C10 CTA modules. An analogue low-pass filter at half the HW sampling frequency is used prior to data sampling in order to avoid aliasing. The probes calibration (fitted to a 4th-order polynomial curve) is performed *in situ* against the Prandtl tube (located at the centerline 7 D upstream

3

the HW rake). The hot-wires are moved to the centerline during calibration.

PIV is used to perform flow-field measurements in a radial streamwise/wall-normal plane. The optical access is provided by two transparent methacrylate windows, placed at the bottom and side accesses (Figure 2). The bottom optical access is used to illuminate a radial vertical plane. The illumination is provided by a double-pulsed Quantel Evergreen Nd:Yag Laser (200 mJ/pulse at 15 Hz). The laser has been placed horizontally below the test section. The light beam is redirected in the vertical direction via a 45°mirror and then shaped into a thin plane using a spherical converging lens and a diverging cylindrical lens. The thickness of the laser sheet is approximately 1 mm. The flow is seeded with 1 μm diameter water/glycol-mixture droplets produced with a Laskin nozzle. The seeding particles are introduced in the most upstream section of the pipe ($\approx 115\ D$ upstream the measurement region) to minimize the perturbation of the flow.

A sCMOS Andor Zyla camera is used as recording device. The camera has a full-frame resolution of 2560×2160 pixels^2, with a pixel size of $6.5 \times 6.5\ \mu$m^2. A 50 mm macro objective, set at numerical aperture of $f/\# = 11$ and equipped with a $0.45\times$ wide angle adapter, is employed to image a region of approximately 27×27 cm^2 with $0.1 < y/R < 0.65$. The camera is placed with a view angle of $\approx 30°$ with respect to the direction normal to the PIV plane; an optical calibration is carried out to obtain a mapping of the local magnification in the laser plane. The procedure is performed before and after each experimental run to assess possible misalignments due to vibrations during the experiments.

The PIV images are pre-processed in order to eliminate background light reflections and improve the image quality using a POD-based filter [35]. In all cases, the subtraction of 10 modes was sufficient to obtain a satisfactory removal of the background contamination. Velocity vector fields are estimated through digital cross-correlation analysis of the particle images [36] with an iterative multi-grid/multi-pass [37] image deformation algorithm [38], with final interrogation windows of 48×48 pixels^2 size and 50% of relative overlap (the final vector spacing is 24 pixels, i.e. ≈ 3 mm in both directions). A validation based on ensemble statistics at each grid point (3 σ criterion) is applied, and the outliers are replaced with an iterative POD-based procedure, similar to the one proposed in Ref. [39]. The vector fields are then spatially re-mapped and corrected taking into account the local magnification and viewing angle and ~~for~~the effects of optical distortion. The relatively small magnification ensures that the errors due to misalignment of the laser sheet and the reference calibration plane are negligible [40].

The PIV acquisition system is controlled with a high-precision pulse generator. The synchronization between PIV and HWA is achieved recording simultaneously the 5 HW signals and the pulse signals corresponding to the PIV laser firing. In total, 6 analog input channels of two NI-9215 modules are used. All the NI modules are mounted on a Ni-cRIO-9068 real-time controller. The acquisition parameters corresponding to each experimental condition are reported in table 1.

2.3. Dynamic estimation of the flow field with extended POD

The procedure for the dynamic estimation of the flow fields is briefly outlined here. The reader is referred to Ref. [28] for a more exhaustive description. The POD snapshot method [41] is first applied both on the PIV and HW datasets. The fluctuating velocity fields are rearranged to form a $N_s \times 2N_p$ snapshot matrix $\boldsymbol{U}_{PIV} = [u, v]$, where N_s is the number of snapshots and N_p is the number of PIV grid points for each velocity component u (streamwise) and v (wall-normal). Similarly, a HW snapshot matrix is built; in order to increase the number of probes, a set of virtual probes is built by assigning to each of the PIV snapshot instants a portion N_t of the HW samples. The probes data matrix $\boldsymbol{U}_{HW}$, consequently, has as many rows as the N_s PIV snapshots, and $N_t \times p$ columns, with N_t being the number of HW samples assigned to each PIV snapshot (see table 2) and p the number of probes. A Singular Value Decomposition (SVD) of the snapshot matrices results in:

$$\begin{cases} \boldsymbol{U}_{PIV} = \boldsymbol{\Psi}_{PIV}\boldsymbol{\Sigma}_{PIV}\boldsymbol{\Phi}_{PIV}^T, \\ \boldsymbol{U}_{HW} = \boldsymbol{\Psi}_{HW}\boldsymbol{\Sigma}_{HW}\boldsymbol{\Phi}_{HW}^T, \end{cases} \quad (1)$$

in which $\boldsymbol{\Psi}$ and $\boldsymbol{\Phi}$ contain the temporal and spatial modes, respectively, of (and form a basis for) the velocity fields and the probe signals, and $\boldsymbol{\Sigma}$ represents the diagonal matrices containing the singular values. The dynamic estimation of the VLSM leverages on the mutual interrelation between the non-time resolved PIV snapshots and the set of data from high speed probes, described by the time correlation matrix between time coefficients of the probe and flow field modes $\boldsymbol{\Psi}_{HW}^T\boldsymbol{\Psi}_{PIV} = \boldsymbol{\Xi}$. The matrix $\boldsymbol{\Xi}$ can be used to provide an LSE of the time-coefficients of the flow field modes given the probe signals time coefficients. This is equivalent to a Multi-Time Delay LSE approach [30, 32]. The snapshot $\boldsymbol{u}_{HW}$ at a generic time instant t can be used to estimate the time coefficients $\hat{\boldsymbol{\psi}}(t)$ and, eventually, the flow fields $\hat{\boldsymbol{u}}(t)$:

$$\begin{aligned} \boldsymbol{\psi}_{HW}(t) &= \boldsymbol{u}_{HW}(t)\boldsymbol{\Phi}_{HW}\boldsymbol{\Sigma}_{HW}^{-1} \\ \hat{\boldsymbol{\psi}}(t) &= \boldsymbol{\psi}_{HW}(t)\boldsymbol{\Xi} \\ \hat{\boldsymbol{u}}(t) &= \hat{\boldsymbol{\psi}}(t)\boldsymbol{\Sigma}_{PIV}\boldsymbol{\Phi}_{PIV}^T, \end{aligned} \quad (2)$$

where the ψ_i elements of each $\boldsymbol{\psi}$ vector are the time coefficients of the ith mode. A crucial step in this process consists in removing spurious contributions due to the uncorrelated part of the probes and velocity field data. [28] proposed to use a 3 σ criterion, i.e. remove all entries Ξ_{ij} with absolute values smaller than 3 times the standard deviation of its rows/columns ($3/\sqrt{N_s}$). The same approach is followed in the present study.
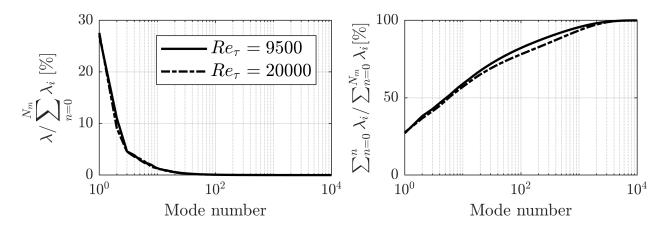
Figure 3: Distribution of POD eigenvalues (left) and their cumulative eigenspectrum (right).

3. Results and discussion

3.1. Modal decomposition of the velocity fields

The POD eigenspectrum is reported in figure 3. Around 27% of the in-plane turbulent kinetic energy is ascribed to the first mode, with barely any visible Reynolds number dependence. Large scale motions (corresponding to the first POD modes, see Ref. 42) contain more than 40% of the turbulent kinetic energy if the modes from 1 to 3 are taken into account.

The spatial modes 1 to 3 are reported in figure 4 for $Re_\tau = 9500$. In agreement with Refs. [42] and [43] for flat plate boundary layers (both with and without pressure gradient), the first spatial mode (figure 4), when combined with a positive time coefficient represents an event with positive streamwise velocity and negative wall-normal velocity which brings high-momentum flow towards the wall, i.e. it is a sweep-like event. However, in equation (2) the flow fields are obtained combining the POD spatial modes multiplied by their associated energy content (POD singular value) and their respective time coefficients. The time-coefficient vector has zero mean, implying that mode 1 represents a sweep-like event whenever multiplied by a positive time coefficient and an ejection-like event whenever multiplied by a negative time coefficient. This is in substantial agreement with what was found in Refs. [44] and [43], i.e. that sweeps and ejections are mirror images of one another; being true for all wall-bounded flows. The proposed definition of sweeps and ejections differs from the classical one based on local quadrant analysis, as it refers explicitly to a certain flow field organization in an extended domain.

The modes from 2 to 3 are correction terms which are needed to determine the radial position and thickness of the sweeps/ejections. In particular, in presence of a sweep, a positive (negative) time coefficient for mode 2 would move the sweep towards (farther away from) the wall. A positive (negative) time coefficient of mode 3 would make the sweep thinner (thicker) in the radial direction. It has

to be noted that modes 3 and 4 share a similar amount of energy. It is not surprising, thus, that for the case at $Re_\tau = 20000$, the energy ranking of these two modes is inverted. According to this description, in the following, sweeps/ejections will be characterized by making use of the modes time coefficients.

3.2. Dynamic estimation of POD time coefficients

Following the methodology proposed in Refs. [28] and summarized in Sec. 2.3, the reconstruction quality is assessed in terms of the determination coefficient:

$$r^2(m) = 1 - \frac{\sum_{i=1}^{N_s} \left(\Psi_{PVIi,m} - \hat{\Psi}_{i,m} \right)^2}{\sum_{i=1}^{N_s} \left(\Psi_{PVIi,m} \right)^2} \ , \quad m = 1, \dots, N_m,$$

(3)

with m indicating the mode number, and i being the generic time instant where original PIV data are available. The matrix $\hat{\Psi}$ contains the estimated time coefficients for in-sample data, i.e. in the same time instants of the PIV snapshots. It is important to remark that, if no filtering is applied to the time-correlation matrix, the extended POD procedure would be equivalent to an LSE [29], thus leading to $r^2 = 1$ for all modes (and consequently not providing any significant information on the reconstruction quality). On the other hand, the application of the filter, as demonstrated in Ref. [28], allows using r^2 as an effective reconstruction quality metric, in addition to the benefit of improving the reconstruction itself in instants between PIV snapshots. The determination coefficient is reported for both tested Reynolds numbers in figure 5; histories of the reconstructed time coefficients for a small portion of the observation time are reported, along with the original PIV time coefficients to benchmark the validity of the reconstruction. If a determination coefficient of 0.4 is set as a minimum quality threshold, for the case with $Re_\tau = 9500$, an acceptable reconstruction is obtained for the first 4 modes, while for $Re_\tau = 20000$, only 3 modes are retained with sufficient accuracy. This is to be ascribed to
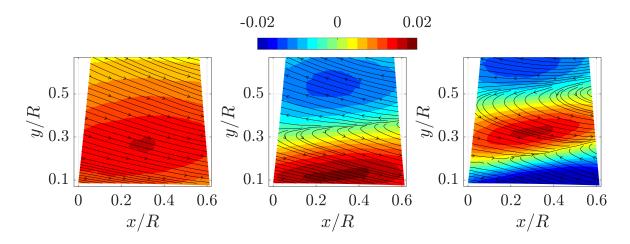
Figure 4: POD spatial modes of the velocity fields (left: 1st; center: 2nd; right 3rd), for the test case with $Re_\tau = 9500$. The contour represents the streamwise velocity component of the POD modes with superposed streamlines indicating the streamwise-radial velocity components.
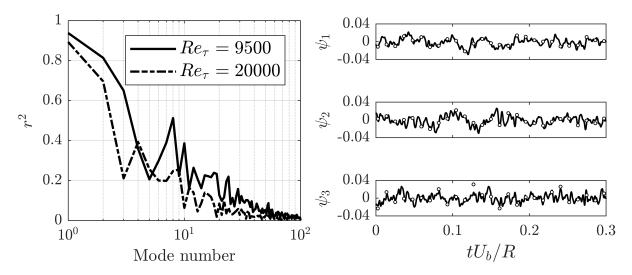

Figure 5: Left panel: determination coefficient for the two test cases. Right panels: dynamic estimation of the time coefficients for the first 3 modes (continuous black line) for a short sequence of the test case with $Re_\tau = 9500$. Circles indicate the time coefficients of the original PIV snapshots.

the larger scale separation, which leads to stronger modulation effects of the PIV data as well as spreading of the energy over a wider spectrum of wavelengths for the higher Re_τ case. This is in line with the cumulative eigenspectrum distribution (Figure 3), which experiences a slower growth for $Re_\tau = 20000$. Additionally, owing to the physical separation between the HW rake and the region of the PIV measurement, the reconstruction favors the modes containing mostly information which is convected downstream. This explains the toothsaw distribution of r^2. Remarkably, the dynamic estimation method extracts convective features, which persist long enough to be detected also by the HW probes, thus retaining large-scale features of the flow field.

Using Taylor's hypothesis, the dynamically-estimated

fields can be used to extract the time/space evolution of these VLSMs. An example of this process is reported in Figure 6 which provides a visual comparison of a large flow field obtained making use of the Taylor hypothesis and employing both time-resolved hot-wire data and reconstructed flow fields. The beneficial effect of the dynamic estimation is of transferring time-resolution from the hot-wire probes to the velocity field measurements; on the downside, the spatial resolution is limited to the largest scales, which are more persistent and, consequently, are highly contributing to the correlation between velocity fields and probe signals. The process is actually filtering the high-frequency part of the spectrum, thus losing information on the small scales. Nonetheless, the comparison of the VLSMs estimated using the hot-wire data and the
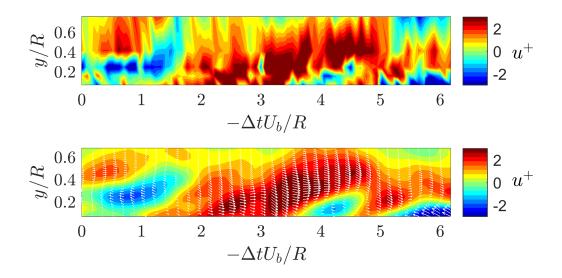
6

Figure 6: Contour of the evolution of the streamwise velocity component obtained using Taylor's hypothesis for the test case with $Re_\tau = 9500$. Top: hot-wire data. Bottom: dynamically-estimated fields. The velocity contours are shown in inner units, i.e. $u^+ = u/u_\tau$.
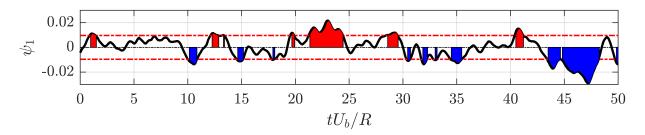

Figure 7: Identification of persistent high/low momentum structures using the first time coefficient. The sequence is from the test case with $Re_\tau = 9500$. Red/blue shadowed areas indicate high/low momentum structures, respectively. Dashed lines indicate the cutoff level to consider the event as high/low momentum.
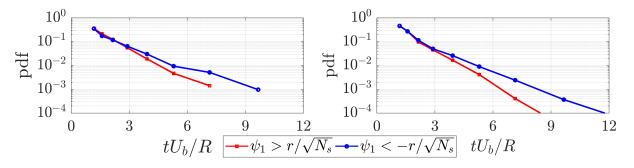

Figure 8: Statistical distribution of large scale motions. Left: $Re_\tau = 9500$. Right: $Re_\tau = 20000$. Events with large positive/negative values of the first time coefficient indicate high/low momentum structures.

dynamically-estimated fields shows that the reconstruction of the large scales is satisfactory.

3.3. Statistical characterization of large scale motions

The results of the POD decomposition suggest that the first mode is largely dominant (independent of the Reynolds number within the explored range), and that it is representative of a sweep/ejection depending on its time coefficient, while the second and third modes contribute in determining position and radial extent of these events. In this scenario, having available the dynamic estimation of the time coefficients, it is possible to identify whether a high momentum (sweep) or low momentum (ejection) structure is occurring by observing the sign of the time co-
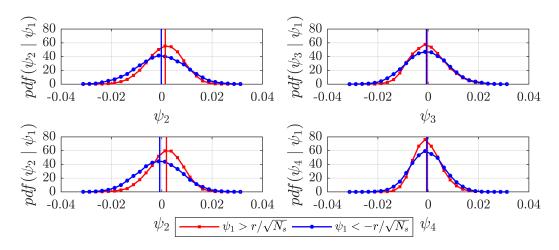
7

Figure 9: Conditional pdf (based on the sign of the LSM detection criterion) of the time coefficients of the $2^{nd}/3^{rd}$ mode (top: $Re_\tau = 9500$) and $2^{nd}/4^{th}$ mode (bottom: $Re_\tau = 20000$). For the case of $Re_\tau = 20000$ the 4th mode has a similar spatial organization of the 3rd mode for $Re_\tau = 9500$, and for this reason it is selected herein for comparison.

efficient of the first mode. The identification of persistent high/low momentum structures is exemplified in Figure 7 on a portion of the time-history of the first time coefficient. In order to extract only significant events to identify the appearance/disappearance of a structure, a threshold (equal to $r/\sqrt{N_s}$, i.e. the standard deviation of the estimated first temporal mode) is applied on the intensity of the time coefficients. To clarify this aspect, Figure 7 visualizes in red the presence of persistent high momentum events (about 3 turnover times in terms of R/U_b, in the middle of the sequence) and in blue low momentum events (about 4 turnover times, at the end of the sequence).

A statistical characterization of these events is carried out. The probability distribution functions (pdf) of the duration of high/low momentum events are shown in Figure 8. Events shorter than 1 turnover time are not included in the statistics. Even though infrequent, it is possible to identify events which persist up to 10 and 13 turnover times for $Re_\tau = 9500$ and 20000, respectively. Low-momentum events are on average longer than high-momentum events, thus suggesting a picture in which ejection-type events are more persistent in time. These findings are in agreement with previous studies in turbulent boundary layers [45] as well as channel and pipe flows [46] at lower Reynolds numbers. This effect seems to be more evident at higher Reynolds number; remarkably, this might be indicative of a broadening of the spectrum of scales involving also the upper end of the spectrum, with more persistent structures of high/low momentum.

The first POD mode locates these high-low momentum events in the region $y/R < 0.4$ (in agreement with Ref. [11]), as shown in Figure 4. Further information on the radial position and radial extent of these high/low momentum events is contained in the 2nd and 3rd mode, respectively. In order to analyze these features, the pdfs of these modes are plotted in Figure 9, conditioned to the events

of occurrence of high-momentum structure ($\hat{\psi}_1 > r/\sqrt{N_s}$) and low-momentum structure ($\hat{\psi}_1 < -r/\sqrt{N_s}$). As mentioned previously, owing to the similarity of the energy content of the 3rd and the 4th mode, small differences lead to an order switch for the case of $Re_\tau = 20000$; for this reason the conditional pdf is evaluated in this case for the 4th mode.

The conditional pdf of the 2nd mode – which modulates the radial position of the LSM events – shows in both cases a skewed distribution towards positive values for the case of high-momentum structures, while for low-momentum structures, the distribution is almost symmetrical around zero. Observing Figure 4, this implies that high-momentum events (sweep-type) occur closer to the wall than low momentum events (ejection-type), which instead maintain their average intensity peak around $y/R = 0.27$. This effect is further intensified as the Reynolds number increases, resulting in sweeps confined to a region even closer to the wall.

The conditional pdf of the 3rd (4th for the case at higher Re_τ) mode – which modulates the radial extent of the LSM events – does not feature any significant asymmetry; nonetheless, the width of the pdf appears larger for the case of low-momentum events, thus testifying that they experience more variability in their radial thickness.

4. Conclusions

The present study reports a high-Reynolds number investigation of Very Large Scale Motions using for the first time for this purpose a combination of synchronized hotwire anemometry and Particle Image Velocimetry with an Extended-POD-based dynamic estimation. This approach gives access to the time history of the POD modes of the velocity fields, which is very difficult to achieve at high Reynolds number. Based on the most energetic

POD modes and on the analysis of the reconstructed time-coefficients, it is possible to define and measure the duration of "global" ejection and sweep-type events, i.e. referring to a certain flow field organization in an extended domain. This provides a more complete view than the commonly used "local" approach based on quadrant analysis applied to single points. Additionally, the method provides a data-driven definition of large-scale-motion (being solely based on the time coefficient of the first POD mode), which is independent of the user input.

The proposed approach demonstrates to be a powerful instrument for the characterization of large-scale coherent motion in pipe flows. It is foreseeable that it could be applied in the most general scenario of wall-bounded turbulence. The advantage of this method is the very limited user input, which renders it a possible candidate for future implementation of flow control approaches based on VLSMs detection.

Conditional statistics on the temporal modes history reveal important features. Firstly, low-momentum large-scale ejections are more frequent and persistent in time than the high-momentum large-scale sweeps. However, both events persists for several – up to 10/12 times – integral time-scales. A second important feature is that the sweep-type structures occur in a region closer to the wall than the ejection-type. These effects are intensified at a higher Reynolds number. Lastly, the radial thickness of the high-momentum events is less variable in time than for low-momentum events, and they tend to occur prevalently close to $y/R \approx 0.25 - 0.30$.

Acknowledgements

References

[1] A. J. Smits, B. J. McKeon, I. Marusic, High–Reynolds number wall turbulence, Annu, Rev. Fluid Mech. 43 (2011) 353–375.

[2] I. Marusic, J. P. Monty, M. Hultmark, A. J. Smits, On the logarithmic region in wall turbulence, J. Fluid Mech. 716 (2013) R3.

[3] H. Nagib, P. Monkewitz, L. Mascotelli, T. Fiorini, G. Bellani, X. Zheng, A. Talamelli, Centerline Kármán "constant" revisited and contrasted to log-layer Kármán constant at CICLoPE, in: 10th International Symposium on Turbulence and Shear Flow Phenomena, Vol. 3, TSFP10, 2017, pp. 7A–3.

[4] P. A. Monkewitz, Revisiting the quest for a universal log-law and the role of pressure gradient in "canonical" wall-bounded turbulent flows, Phys. Rev. Fluids 2 (2017) 094602.

[5] P. Luchini, Universality of the turbulent velocity profile, Phys. Rev. Lett. 118 (2017) 224501.

[6] C. E. Willert, J. Soria, M. Stanislas, J. Klinner, O. Amili, M. Eisfelder, C. Cuvier, G. Bellani, T. Fiorini, A. Talamelli, Near-wall statistics of a turbulent pipe flow at shear Reynolds numbers up to 40000, J. Fluid Mech. 826 (2017) R5.

[7] R. Örlü, T. Fiorini, A. Segalini, G. Bellani, A. Talamelli, P. H. Alfredsson, Reynolds stress scaling in pipe flow turbulence-first results from CICLoPE, Phil. Trans. R. Soc. A 375 (2017) 20160187.

[8] R. Mathis, N. Hutchins, I. Marusic, Large-scale amplitude modulation of the small-scale structures in turbulent boundary layers, J. Fluid Mech. 628 (2009) 311–337.

[9] P. H. Alfredsson, R. Örlü, A. Segalini, A new formulation for the streamwise turbulence intensity distribution in wall-bounded turbulent flows, Eur. J. Mech.-B/Fluids 36 (2012) 167–175.

[10] B. Ganapathisubramani, E. K. Longmire, I. Marusic, Characteristics of vortex packets in turbulent boundary layers, J. Fluid Mech. 478 (2003) 35–46.

[11] K. Kim, R. Adrian, Very large-scale motion in the outer layer, Phys. Fluids 11 (1999) 417–422.

[12] M. Guala, S. E. Hommema, R. J. Adrian, Large-scale and very-large-scale motions in turbulent pipe flow, J. Fluid Mech. 554 (2006) 521–542.

[13] J. Monty, J. Stewart, R. Williams, M. Chong, Large-scale features in turbulent pipe and channel flows, Journal of Fluid Mechanics 589 (2007) 147–156.

[14] B. Balakumar, R. Adrian, Large-and very-large-scale motions in channel and boundary-layer flows, Philosophical Transactions of the Royal Society of London A: Mathematical, Physical and Engineering Sciences 365 (1852) (2007) 665–681.

[15] A. A. Townsend, The structure of turbulent shear flow, Cambridge University Press, 2nd ed.

[16] I. Marusic, J. P. Monty, Attached Eddy Model of Wall Turbulence, Annu. Rev. Fluid Mech. 51.

[17] M. de Giovanetti, Y. Hwang, H. Choi, Skin-friction generation by attached eddies in turbulent channel flow, J. Fluid Mech. 808 (2016) 511–538.

[18] N. Hutchins, I. Marusic, Large-scale influences in near-wall turbulence, Philosophical Transactions of the Royal Society of London A: Mathematical, Physical and Engineering Sciences 365 (2007) 647–664.

[19] I. Marusic, B. J. McKeon, P. A. Monkewitz, H. M. Nagib, A. J. Smits, K. R. Sreenivasan, Wall-bounded turbulent flows at high Reynolds numbers: recent advances and key issues, Phys. Fluids 22 (2010) 065103.

[20] M. R. Abbassi, W. J. Baars, N. Hutchins, I. Marusic, Skin-friction drag reduction in a high-Reynolds-number turbulent boundary layer via real-time control of large-scale structures, Int. J. Heat Fluid Fl. 67 (2017) 30–41.

[21] R. Mathis, N. Hutchins, I. Marusic, A predictive inner–outer model for streamwise turbulence statistics in wall-bounded flows, J. Fluid Mech. 681 (2011) 537–566.

[22] R. J. Adrian, Hairpin vortex organization in wall turbulence, Physics of Fluids 19 (4) (2007) 041301.

[23] O. Flores, J. Jimenez, Effect of wall-boundary disturbances on turbulent channel flows, Journal of Fluid Mechanics 566 (2006) 357–376.

[24] O. Flores, J. Jimenez, J. C. Del Alamo, Vorticity organization in the outer layer of turbulent channels with disturbed walls, Journal of Fluid Mechanics 591 (2007) 145–154.

[25] L. H. O. Hellström, B. Ganapathisubramani, A. J. Smits, The evolution of large-scale motions in turbulent pipe flow, J. Fluid Mech. 779 (2015) 701–715.

[26] L. H. O. Hellström, I. Marusic, A. J. Smits, Self-similarity of the large-scale motions in turbulent pipe flow, J. Fluid Mech. 792.

[27] S. Discetti, F. Coletti, Volumetric velocimetry for fluid flows, Measurement Science and Technology 29 (2018) 042001.

[28] S. Discetti, M. Raiola, A. Ianiro, Estimation of time-resolved turbulent fields through correlation of non-time-resolved field measurements and time-resolved point measurements, Exp. Therm. Fluid Sci. 93 (2018) 119–130.

[29] J. Borée, Extended proper orthogonal decomposition: a tool to analyse correlated events in turbulent flows, Exp. Fluids 35 (2003) 188–192.

[30] D. Ewing, J. H. Citriniti, Examination of a LSE/POD complementary technique using single and multi-time information in the axisymmetric shear layer, in: IUTAM Symp. on simulation and identification of organized structures in flows, Springer, 1999, pp. 375–384.

[31] C. Tinney, F. Coiffet, J. Delville, A. Hall, P. Jordan, M. Glauser, On spectral linear stochastic estimation, Experiments in fluids 41 (2006) 763–775.

[32] C. E. Tinney, L. S. Ukeiley, M. N. Glauser, Low-dimensional characteristics of a transonic jet. Part 2. Estimate and far-field prediction, J. Fluid Mech. 615 (2008) 53–92.

[33] G. Bellani, Talamelli, The final design of the long pipe in CIC-LOPE, Progress in Turb. VI (2016) 205–209.

[34] T. Fiorini, Turbulent pipe flow-high resolution measurements in ciclope, Ph.D. thesis, Alma Mater Studiorum - Universitá di Bologna (2017).

[35] M. A. Mendez, M. Raiola, A. Masullo, S. Discetti, A. Ianiro, R. Theunissen, J.-M. Buchlin, POD-based background removal for particle image velocimetry, Exp, Therm. Fluid Sci. 80 (2017) 181–192.

[36] C. E. Willert, M. Gharib, Digital particle image velocimetry, Exp. Fluids 10 (1991) 181–193.

[37] J. Soria, An investigation of the near wake of a circular cylinder using a video-based digital cross-correlation particle image velocimetry technique, Experimental Thermal and Fluid Science 12 (1996) 221–233.

[38] F. Scarano, Iterative image deformation methods in PIV, Meas. Sci. Technol. 13 (2001) R1–R19.

[39] S. G. Raben, J. J. Charonko, P. P. Vlachos, Adaptive gappy proper orthogonal decomposition for particle image velocimetry data reconstruction, Meas. Sci. Technol. 23 (2012) 025303.

[40] S. Discetti, R. J. Adrian, High accuracy measurement of magnification for monocular PIV, Measurement Science and Technology 23 (2012) 117001.

[41] L. Sirovich, Turbulence and the dynamics of coherent structures. I. Coherent structures, Quart. Appl. Math. 45 (1987) 561–571.

[42] Y. Wu, A study of energetic large-scale structures in turbulent boundary layer, Phys. Fluids 26 (2014) 045113.

[43] C. Sanmiguel Vila, R. Örlü, R. Vinuesa, P. Schlatter, A. Ianiro, S. Discetti, Adverse-pressure-gradient effects on turbulent boundary layers: Statistics and flow-field organization, Flow Turbul. Combust. 99 (2017) 589–612.

[44] A. Lozano-Durán, J. Jiménez, Effect of the computational domain on direct simulations of turbulent channels up to $Re_\tau =$ 4200, Phys. Fluids 26 (2014) 011702.

[45] J. A. Sillero, J. Jiménez, R. D. Moser, Two-point statistics for turbulent boundary layers and channels at Reynolds numbers up to $\delta^+ \approx 2000$, Phys. Fluids 26 (2014) 105109.

[46] J. H. Lee, H. J. Sung, Comparison of very-large-scale motions of turbulent pipe and boundary layer simulations, Phys. Fluids 25 (2013) 045103.